



The evolution of saponite: An experimental study based on crystal chemistry and crystal growth

Chaoqun Zhang, Hongping He, Sabine Petit, Fabien Baron, Q I Tao, Brian Gregoire, Jianxi Zhu, Yiping Yang, Shichao Ji, And Shangying Li

► To cite this version:

Chaoqun Zhang, Hongping He, Sabine Petit, Fabien Baron, Q I Tao, et al.. The evolution of saponite: An experimental study based on crystal chemistry and crystal growth. The American Mineralogist, 2020, 10.2138/am-2021-7625 . hal-03006209

HAL Id: hal-03006209

<https://hal.science/hal-03006209>

Submitted on 15 Nov 2020

HAL is a multi-disciplinary open access archive for the deposit and dissemination of scientific research documents, whether they are published or not. The documents may come from teaching and research institutions in France or abroad, or from public or private research centers.

L'archive ouverte pluridisciplinaire **HAL**, est destinée au dépôt et à la diffusion de documents scientifiques de niveau recherche, publiés ou non, émanant des établissements d'enseignement et de recherche français ou étrangers, des laboratoires publics ou privés.

Revision 1

The evolution of saponite: An experimental study based on crystal chemistry and crystal growth

CHAOQUN ZHANG^{1, 2, 3}, HONGPING HE^{1, 3, *}, SABINE PETIT^{2, *}, FABIEN BARON²,
 QI TAO¹, BRIAN GREGOIRE², JIANXI ZHU^{1, 3}, YIPING YANG^{1, 3}, SHICHAO JI^{1, 3},
 AND SHANGYING LI^{1, 3}

¹ CAS Key Laboratory of Mineralogy and Metallogeny/Guangdong Provincial Key
 Laboratory of Mineral Physics and Materials, Guangzhou Institute of Geochemistry,
 Chinese Academy of Sciences, Guangzhou 510640, China

² Institut de Chimie des Milieux et Matériaux de Poitiers (IC2MP), UMR 7285 CNRS,
 Université de Poitiers, F-86073 Poitiers Cedex 9, France

³ University of Chinese Academy of Sciences, Beijing 100049, China

Corresponding Authors

Prof. Hongping He

Present address:

Guangzhou Institute of Geochemistry, Chinese Academy of Sciences,
 Guangzhou 510640, China.

*E-mail: hehp@gig.ac.cn

Prof. Sabine PETIT

Present address:

UMR 7285 CNRS, Université de Poitiers, F-86073 Poitiers Cedex 9, France.

23 *E-mail: sabine.petit@univ-poitiers.fr

ABSTRACT

Element incorporation and partitioning during the evolution of clay minerals have significant implications for element cycling in geochemical processes. The main aim of this experimental study is to expand our understanding of element redistribution and crystal growth during smectite evolution under different physicochemical conditions. The precursors (i.e., pure Mg- and Ni-saponite) were separately prepared by hydrothermal syntheses at the same set of temperatures (i.e., RT, 50, 150, 180, 200, and 220 °C) for one day. Then the starting materials were obtained from the mechanical mixtures of the identical molar weight of Mg- and Ni-smectite precursors prepared at the same temperature. Subsequently, Series I samples were obtained by hydrothermally treating different starting materials at 220 °C for two weeks while Series II samples were hydrothermally synthesized under various temperatures (220, 300, 400, and 500 °C) for one week by using the starting materials prepared at 220 °C. Both the precursors and the resultant saponites were characterized by XRD, FTIR, TEM, and STEM. The FTIR spectra of the precursors only exhibit the $\nu\text{Mg}_3\text{OH}$ and $\nu\text{Ni}_3\text{OH}$ bands, corresponding to Mg-saponite and Ni-saponite, respectively. However, the occurrence of $\nu\text{Mg}_2\text{NiOH}$ and $\nu\text{Ni}_2\text{MgOH}$ bands in the resultant saponite indicates the dissolution of the corresponding Mg- and Ni-saponite precursors and recrystallization of Mg-Ni mixed saponite. The dissolution extents of Mg- and Ni-saponite precursors, which affect the degrees of random distribution of octahedral Ni and Mg in resultant Mg,Ni-saponite, are significantly controlled by the temperature gap (ΔT) between the precursors prepared and the resultant Mg,Ni-saponite obtained. In general, a larger ΔT leads to a higher dissolution extent of saponite precursors and a higher degree of random distribution of

octahedral Ni and Mg cations in the resultant Mg,Ni-saponite. Thus, the distribution mode of octahedral cations in saponite, which is not only relevant to a given hydrothermal temperature but also dependent on ΔT for final products, cannot be used as a geothermometer. TEM and STEM observations provide visual evidence that the particles of saponite coarsen when ΔT is higher than zero. Both the crystal-chemistry and morphological features during saponite evolution suggest that saponite particles coarsen mainly via partial/complete dissolution of precursors followed by recrystallization and growth of Mg,Ni-saponite, in which crystal growth by layer attachment cannot be excluded. This study presents an experimental model to evaluate the evolution of clay minerals by crystal-chemistry and crystal growth and offers a better understanding of the contributions of clay mineral evolution to the element cycling.

Keywords: smectite, crystal growth, crystal chemistry, cation distribution, clay evolution

INTRODUCTION

Smectites, which are ubiquitous on Earth's surface, have received particular attention because of their geochemical significance and wide applications in industry (Brigatti et al., 2013). At and near the surface of the Earth, smectites can survive over a wide range of temperature, pressure, and solution concentration conditions (Tardy et al., 1987). They can form via weathering as well as diagenesis and hydrothermal alteration of volcanic glass and other rocks (Eberl, 1984; Merriman, 2005; Voigt et al., 2020). These formation pathways usually involve a crucial process, element incorporation and partitioning during smectite growth (Christidis and Huff, 2009; Hazen et al., 2013). Thus, smectite is not only a reactive template but also a metastable component that will transform into other minerals in nature. Their evolution is of great importance in understanding geochemical behaviors of elements and related mineralization in hypergenic processes, as well as inferring paleo-environment changes in the Earth's history (Galán and Ferrell, 2013).

Weathering usually yields non-crystalline or nanoparticle smectites, which tend to grow into larger smectite particles when exposed to diagenetic-hydrothermal environments or buried in sedimentary environments. These processes result in variations in crystal-chemistry and morphology of smectite, due to physicochemical condition changes that frequently occur in natural systems (Eberl, 1984; Merriman, 2005; Galán and Ferrell, 2013). Previous studies have reported that smectites evolve from poorly crystalline precursors in various environments (Zhou and Fyfe, 1989; Banfield and Eqqleton, 1990; Kawano and Tomita, 1992; Christidis, 2001; Christidis and Huff, 2009; Baldermann et al., 2015; Cuadros et al., 2017; Zhang et al., 2020), which is important for

the geochemical budget for the elements such as Si, Al, Fe, and Mg. However, literature dedicated to such evolution mainly focused on the alterations of primary minerals into smectites instead of the evolution of smectites themselves. So far, very limited studies have been devoted to the cognition of smectite self-evolution (Christidis, 2001; Baldermann et al., 2015; Zhang et al., 2020). Christidis (2001) attempted to develop the growth patterns of natural smectite via morphological analyses. Baldermann et al. (2015) have reported on the evolution of particle size and crystal chemistry of synthetic Fe/Mg-saponite. Recently, we highlighted the growth kinetics of smectite by investigating cation distribution and morphology evolution (Zhang et al., 2020). These studies have greatly enhanced our understanding of smectite evolution, but many questions remain unanswered. One of these questions is how the cation distribution and morphology of smectites evolve under different physicochemical conditions.

In view of uncontrollable compositions of natural smectites and mature researches about smectite synthesis (Kloprogge et al., 1999; Zhang et al., 2010; Petit et al., 2017), we chose synthetic smectites as the research objects and focused on their crystal chemistry and morphology under different physicochemical conditions to answer the question mentioned above. Saponite is easy-synthesized tri-octahedral smectite, with ideal structural formula $\text{Na}_x[\text{Si}_{4-x}\text{Al}_x][\text{M}_3]\text{O}_{10}(\text{OH})_2 \cdot n\text{H}_2\text{O}$, where M corresponds to divalent cations; x is the fraction of aluminum present in the tetrahedral sheet (generally $0.3 \leq x \leq 0.6$); Na is the interlayer cation compensating the tetrahedral charge; and n is the number of interlayer water molecules (Brigatti et al., 2013). In the octahedral sheet, each OH group is linked to three neighboring M atoms, which allows systematically investigating the octahedral cations distribution in clay minerals via recording the

stretching vibration of structural OH (Petit and Madejová, 2013). Hence, the synthesis of saponite is advantageous to investigate smectite evolution, notably during the early-stage growth, which is scarcely observed in nature. Based on our previous study about morphology and crystal-chemistry of saponite with the change of hydrothermal time (Zhang et al., 2020), we further expand on the evolution trend of saponite by using the parameters of crystal-chemistry and crystal growth of saponite with the change of hydrothermal temperature in present study. The Mg- and Ni- saponite system was chosen as the study of object because they can be easily synthesized. Meanwhile, Mg-saponite and Ni-saponite have very similar structure due to the similar radii of Ni^{2+} and Mg^{2+} whereas the different atomic mass of Mg and Ni are meaningful to perform crystal-chemistry analysis. Two series of saponites were hydrothermally synthesized. Series I was obtained by hydrothermal treating different starting materials previously formed at various temperatures (RT, 50, 150, 180, 200, and 220 °C) at 220 °C for two weeks. Whereas the Series II was obtained by hydrothermal treating the same starting material synthesized at 220 °C for one week at various temperatures (220, 300, 400, and 500 °C). The crystal-chemistry, including chemical composition and ions distribution, was characterized by Fourier Transform Infrared (FTIR), X-ray energy-dispersive spectroscopy (EDS), and High-angle annular dark-field scanning transmission electron microscopy (HAADF-STEM). The morphology related to the crystal growth was investigated by transmission electron microscopy (TEM).

MATERIALS AND METHODS

Synthesis of Mg- and Ni-saponite precursors

Mg- and Ni-saponite precursors were prepared using the method described by He et al. (2014). The co-precipitated gel with a theoretical molar ratio of Si:Al:Mg = 3.7:0.3:3 was obtained by mixing solutions of $\text{Na}_2\text{SiO}_3 \cdot 5\text{H}_2\text{O}$, $\text{AlCl}_3 \cdot 6\text{H}_2\text{O}$ and $\text{MgCl}_2 \cdot 6\text{H}_2\text{O}$. Then, the gel was collected by filtration and gently washed with deionized water to remove the excess of salt. The wet gel was transferred to a polytetrafluoroethylene-lined autoclave, and 30 ml of deionized water was added into the autoclave. The resultant mixture was hydrothermally treated at different temperatures (RT, 50, 150, 180, 200, and 220 °C) for one day under equilibrium vapor pressure. The hydrothermal products, named as pMgx (x= gel, 50, 150, 180, 200, and 220), were obtained after filtration and dried at 45°C. Ni-saponite precursors were prepared by using the same method as above-mentioned with $\text{NiCl}_2 \cdot 6\text{H}_2\text{O}$ added instead of $\text{MgCl}_2 \cdot 6\text{H}_2\text{O}$. The resultant products were named as pNix (x= gel, 50, 150, 180, 200, and 220). The chemical formulae for Mg-saponite and Ni-saponite precursors can be expressed as $(\text{Si}_{3.7}\text{Al}_{0.3})^{\text{IV}}(\text{Mg}_3)^{\text{VI}}\text{O}_{10}(\text{OH})_2 \cdot 0.3\text{Na}^+$ and $(\text{Si}_{3.7}\text{Al}_{0.3})^{\text{IV}}(\text{Ni}_3)^{\text{VI}}\text{O}_{10}(\text{OH})_2 \cdot 0.3\text{Na}^+$, respectively, based on their chemical compositions (He et al., 2014).

Synthesis of Mg,Ni-saponite

In the syntheses of Mg,Ni-saponite samples, the starting material was prepared by mixing an identical molar weight of Mg- and Ni-saponite precursors synthesized at the same temperature (e.g., pMg150 and pNi150). The detailed experimental procedure is as follows: the mixture of 0.11g Mg-saponite precursor (pMgx) and 0.14 g Ni-saponite precursor (pNix) was added to 30 ml of deionized water at room temperature and kept continuous stirring for one day for complete dispersion. By using the same method, a set of mixtures were prepared, i.e., the mixtures of pMg-gel and pNi-gel, pMg50 and pNi50,

pMg150 and pNi150, pMg180 and pNi180, pMg200 and pNi200, and pMg220 and pNi220. These mixtures were used as the starting materials for further syntheses of Mg,Ni-saponite under different hydrothermal conditions.

Syntheses of Series I samples. Every mixture was transferred to a polytetrafluoroethylene-lined autoclave and treated at 220 °C for two weeks (Table 1). The products were washed by deionized water, collected by filtration, and dried at 45 °C. The obtained samples were named as T-220, where T stands for the temperature in precursor preparation. For example, sample 150-220 means that the saponite was synthesized at 220 °C, using the Mg- and Ni-saponite precursors that were prepared at 150 °C as starting materials.

Syntheses of Series II samples. Four identical mixtures of pMg220 and pNi220 were prepared as the above-mentioned method. Each mixture containing 30 ml of deionized water was transferred to a 56 ml volume gold tube, sealed by using high-temperature flame. Then, these sealed gold tubes were put into the high-temperature heating jackets that were pre-set at different temperatures (220, 300, 400, and 500 °C) and were heated for one week. The obtained products were washed by filtration, dried at 45 °C, and named as 220-T (T stands for the hydrothermal temperature of the product).

Analysis methods

X-ray diffraction. Powder X-ray diffraction (XRD) patterns were obtained on a Bruker D8 advance diffractometer (CuK α radiation, 40 kV and 40 mA) over the range of 2-65° (2 θ) with 0.025° (2 θ) step size and 0.6 s per step, while the patterns of the oriented samples and glycolated samples were collected over the range of 2-15° (2 θ). The randomly oriented samples were prepared by pressing saponite powder inside a cavity up

to the reference level of the sample holders. The oriented samples were prepared by carefully pipetting the clay suspension onto a glass slide and allowing it to dry at ambient temperature. Glycolated samples were prepared by treating the oriented samples in a glass desiccator with ethylene glycol at 20 °C for 24 h.

FTIR spectra. Fourier Transform Infrared (FTIR) spectroscopy is available to study the growth process of saponite by a crystal-chemistry approach. Because OH vibrations are affected by octahedral cations to which the OH group is coordinated, the structural OH stretching vibration (νOH) bands allow probing the octahedral environment (Petit and Madejová, 2013). Thus, the νOH bands in the middle infrared (MIR) region can be used to determine the crystal-chemistry associated with the evolution process of saponite. In this study, a Magna-IR 6700 Nicolet spectrometer was used for MIR spectra over the range 400–4000 cm^{-1} , with an EverGlo source, a CsI beam splitter, a DTGS-CsI detector and a resolution of 4 cm^{-1} with co-additions of 100 scans. MIR spectra were obtained in transmission through KBr pellets, prepared with 1 mg of sample and 150 mg of KBr salt. The mixture was pressed for 5 min at 8 kbar and dried overnight in an oven at 150 °C. Spectral manipulations were performed using the OMNIC software package. To determine the octahedral cation distribution in the synthesized saponites, decomposition and curve-fitting have been used to obtain the integrated intensities (S) of the different OH-stretching bands. The S of the bands is proportional to the concentration of absorbing centers of the given OH types, assuming that the absorption coefficients are constant for all metal OH stretching vibration bands (e.g., Slonimskaya et al., 1986; Petit et al., 2004; Madejová et al., 2017). The decomposition of the spectral envelop into bands was undertaken by the Peakfit software package, using four Gauss–Lorentz cross-product

functions corresponding to the four possible environments associated with structural OH stretching vibrations (Mg_3OH , Mg_2NiOH , MgNi_2OH , and Ni_3OH). The experimental spectra were iteratively fitted by fixing the four central positions of four frequencies of structural OH stretching vibrations until the squared correlation coefficients $r^2 \geq 0.995$. Then, the band positions and area were extracted. The degree of random distribution of octahedral cations in octahedral sheet of the synthesized saponites ($R_{(\text{IR})}$) was measured by the ratio of the S of the bands that involve neighboring Mg and Ni cations to the total S of the structural OH stretching vibrations, i.e., $R_{(\text{IR})} = (\text{SvMg}_2\text{NiOH} + \text{SvNi}_2\text{MgOH}) / (\text{SvMg}_3\text{OH} + \text{SvMg}_2\text{NiOH} + \text{SvNi}_2\text{MgOH} + \text{SvNi}_3\text{OH})$. When the same number of Mg and Ni randomly distributes in three vacancies around structural OH, the corresponding theoretical ratio is 0.125 for Mg_3OH and 0.125 for Ni_3OH , 0.375 for Mg_2NiOH and 0.375 for Ni_2MgOH ; thus $R_{(\text{theory})}$ equals 0.75 (Zhang et al., 2020). Correspondingly, the dissolution extent (i.e., the dissolution ratio of precursors) can be estimated by $R_{(\text{IR})}/R_{(\text{theory})}$.

STEM-EDS. High-angle annular dark-field scanning transmission electron microscopy (HAADF-STEM) observations were performed to investigate the morphology in the *ab* direction of the saponite particles. 1 mg sample was soaked into 10 ml deionized water with slightly stirring for one week to obtain a dilute colloidal suspension. Specimens were prepared by dispersing the colloidal suspension in 40 ml ethanol and ultrasonically treating for 30 min. A drop of the resultant suspension was placed on a porous carbon film supported by a copper grid, then the water and ethanol were evaporated. STEM images were obtained using a FEI Talos F200S high-resolution transmission electron microscope (HRTEM) operated at 200 kV. For the HRTEM

investigation of the particle size and the lattice fringe along the [001] direction, oriented samples were embedded in epoxy resin for the preparation of ultrathin sections. Subsequently, ultrathin sections (~50 nm) were obtained using an ultramicrotome (Lecia EM UC7) with a diamond knife and transferred onto holey carbon-coated TEM copper grids. HRTEM images and X-ray energy-dispersive spectroscopy (EDS) were carried out using a FEI Talos F200S high-resolution transmission electron microscope equipped with Super-X X-ray spectroscopy and operated at 200 kV. The beam diameter for EDS analyses is about 5 nm. The relative contents of Mg and Ni were collected from ultrathin-section samples by STEM-EDS as follows: the contents of Mg and Ni at different positions within one particle was measured, plotting the corresponding Mg/(Mg + Ni) value on the graph to obtain a variation trend. Then variation trends of Mg/(Mg + Ni) of numerous randomly selected particles from one sample were summarized into one graph.

RESULTS

Mg- and Ni-saponite precursors

Powder XRD patterns of the Mg- and Ni-saponite precursors display characteristic reflections of trioctahedral smectites with the (001) reflection at ~1.25 nm, the (06,33) at 0.153 nm and asymmetric (*hk*) bands (Fig. 1) (Brindley, 1966; Borchardt, 1989). The reflections of the saponite precursors became narrow and symmetric with the increase of hydrothermal temperatures. For the precursors synthesized below 50 °C, unrecognized reflections suggest that the products are non-crystalline. For the products synthesized between 50 and 180 °C, weak and broad reflections of (02,11), (13,20), and (06,33) were recorded, whereas the (001) basal reflection was still not well recognized. This suggests the formation of TOT layers of saponite but poor layer stacking along the *c*

direction. However, when the hydrothermal temperature increased to 200 °C, both distinct (001) reflection and the reflections related to *ab* planes were exhibited, indicating the formation of well-crystallized saponite. Both the evolutions of Mg- and Ni-saponite precursors are similar, consistent with those reported in the literature (Decarreau et al., 2008; Petit et al., 2008; He et al., 2014).

The FTIR spectra of the synthetic precursors are also similar to those reported in the literature for Ni- and Mg-saponites (Zhang et al., 2020). The band at 3678 cm⁻¹ in all Mg-saponite precursors (Fig. 2a) and 3629 cm⁻¹ in all Ni-saponite precursors (Fig. 2b) are assigned to the stretching vibrations of Mg₃OH (ν Mg₃OH) and Ni₃OH (ν Ni₃OH), respectively. Both the bands tend to become narrower and more intense with the increase of hydrothermal temperature. Concomitantly, the broad band (centered at ~ 3420 cm⁻¹), corresponding to the OH stretching vibration of water molecules, decreases (Fig. 2). The evolution of the width and the intensity of the structural OH vibrations with the hydrothermal treatment temperature suggests that a high temperature favours the crystallization of saponite precursors, consistent with the XRD results. Note that the Al occupancy in the synthetic saponites has been delicately studied in a previous paper (He et al., 2014). The results indicate that Al prefers to occupy tetrahedral sites rather than octahedral sites, and little Al occurs in the octahedral sheets of saponite precursors.

Mg,Ni-saponites in Series I

The XRD patterns of the oriented samples display the characteristic reflections of saponites with a basal spacing at ~ 1.24 nm, which shifts to 1.72 nm after exposure to ethylene glycol (Fig. 3a) (Suquet et al., 1981; Borchardt, 1989). The ethylene glycolated samples exhibit rational *00l* reflections, representative of the periodic structure of

saponite without any interstratified talc-like layers. The intensity of the basal reflections of samples gel-220, 50-220, and 150-220 is higher than that of samples 180-220, 200-220, and 220-220, suggesting the layer stacking in the former (i.e., samples gel-220, 50-220, and 150-220) is more ordered than that in the latter (i.e., samples 180-220, 200-220, and 220-220).

In clay minerals, the OH stretching vibrations are closely associated with the octahedral cations that are coordinated to the hydroxyl groups. For the Mg,Ni-saponite synthesized in the present study, up to four OH stretching vibrations with different wavenumbers (i.e., 3675, 3663, 3648, and 3628 cm^{-1}) can be distinguished, depending on the distribution of Mg^{2+} and Ni^{2+} in octahedral sites. These vibrations correspond to the four possible combinations of the two different cations distributed in the three octahedral sites within one structural unit, i.e., Mg_3OH , Mg_2NiOH , MgNi_2OH , and Ni_3OH (Zhang et al., 2020). In the FTIR spectrum of sample 220-220 of which the temperatures for the precursors' syntheses and subsequent hydrothermal treatment are the same (i.e., the temperature gap, ΔT , is zero), only two prominent vibrations are recorded at 3675 and 3628 cm^{-1} , attributed to $\nu\text{Mg}_3\text{OH}$ and $\nu\text{Ni}_3\text{OH}$, respectively (Fig. 4a). However, with an increase of the temperature gap (ΔT) from sample 200-220 to gel-220, four OH stretching vibrations at 3675, 3663, 3648, and 3628 cm^{-1} were displayed with a prominent intensity decrease of $\nu\text{Mg}_3\text{OH}$ and $\nu\text{Ni}_3\text{OH}$ and a simultaneous intensity increase of $\nu\text{Mg}_2\text{NiOH}$ and $\nu\text{MgNi}_2\text{OH}$. For samples 50-220 and gel-220, the band intensities of $\nu\text{Mg}_2\text{NiOH}$ and $\nu\text{MgNi}_2\text{OH}$ are much stronger than those of $\nu\text{Mg}_3\text{OH}$ and $\nu\text{Ni}_3\text{OH}$.

HRTEM images of ultrathin sections of both the precursors and the corresponding synthetic Mg,Ni-saponites provide information about particle size and layer stacking

(dis)order of saponite (Fig. 5). The precursors prepared at different temperatures display a prominent variation in particle size. For pMg50 and pNi50 precursors, no well-ordered layer stacking was observed, which is consistent with the unresolved (001) reflections in their XRD patterns (Fig. 5a and b). For the precursors synthesized at higher temperatures (e.g., 150 and 180 °C), the layer structure is recognizable. For example, in the case of the precursors synthesized at 150 °C (Fig. 5d and e), the lengths of particles along the *a*- or *b*-axis are approximately 5 - 30 nm, while the heights along *c*-axis is about 1 - 6 nm (i.e., 1 - 4 layers). The few numbers of stacking layers and widespread monolayers of such precursors may lead to the absence of (001) reflections in their XRD patterns. The height/length refer mainly to the size of bundles of saponite particles rather than truly the size of individual particles because the dispersion of the samples was not complete. With the rise of hydrothermal temperature, both the height and length of precursor particles increase (Fig. 5g and h). Note that, after hydrothermally treated at 220 °C for all the precursors prepared at a low temperature (e.g., gel-220, 150-220 and 180-220), lattice-fringe images show that the resultant Mg,Ni-saponites consist of bulk crystals with 5 - 15 layers along the *c*-axis and 40 - 150 nm in length (Fig. 4c, f and i). The crystal size of the resultant saponite is much larger than that of their corresponding precursors, which indicates crystal growth taking place during the hydrothermal treatment.

A summarization of the Mg/(Mg + Ni) ratios at different positions within a sample can provide evidence for the statistical distribution of Mg and Ni cations. In such cases, the more the number of points measured, the more reliable the statistical information of cation distribution will be. Figure 6 shows our STEM-EDS analyses that were conducted on a randomly selected particle in the ultrathin section of sample gel-220

(Fig. 6a) and the $\text{Mg}/(\text{Mg}+\text{Ni})$ ratios obtained from different positions (Fig. 6b). Our measurements show that, in general, the $\text{Mg}/(\text{Mg}+\text{Ni})$ ratios obtained from different points of one sample were located within a certain value. For instance, the $\text{Mg}/(\text{Mg}+\text{Ni})$ ratios of sample gel-220 were located around 0.5 (Fig. 6), suggesting a random distribution of both Mg and Ni within the saponite. In the same way, a ratio of 1 for $\text{Mg}/(\text{Mg}+\text{Ni})$ means that all the octahedral sites in the measured saponite are occupied by Mg (i.e., Mg-saponite) while a ratio of 0 reflects that all the octahedral sites are occupied by Ni (i.e., Ni-saponite). Figure 7 exhibits a summary of the $\text{Mg}/(\text{Mg}+\text{Ni})$ ratios for saponites prepared from different precursors. For sample gel-220 that was synthesized at 220 °C by using Mg- and Ni-bearing gel, the $\text{Mg}/(\text{Mg}+\text{Ni})$ ratios well locate around 0.5 (Fig. 7a), indicating that both Mg and Ni are randomly distributed within the saponite. In the case of sample 150-220 (Fig. 7b), the $\text{Mg}/(\text{Mg} + \text{Ni})$ ratios slightly deviate from 0.5 but lower than 0.75, implying that the distribution of most Ni and Mg cations is random but small clusters of Mg- and Ni- saponite may occur in the sample. Note that Figure 7c displays the $(\text{Mg}/\text{Mg}+\text{Ni})$ ratios measured on fifteen randomly selected particles in sample 180-220, and for each particle, at least five points were measured along layer direction. For this sample, the $\text{Mg}/(\text{Mg}+\text{Ni})$ ratios obviously deviate from the value of 0.5 and shift to 0 or 1 (Fig. 7c). Such $\text{Mg}/(\text{Mg}+\text{Ni})$ ratios suggest that domains of Mg- and Ni-saponite occur in the resultant saponite.

Mg,Ni-saponites in Series II

XRD patterns of the resultant saponites in Series II display characteristic (001) reflections at 1.20 nm, which shifts to ~1.72 nm upon ethylene glycolation (Fig. 3b). For the oriented samples, the width of the basal reflections tends to decrease with the increase

of the synthesis temperature. For the case of sample 220-500, broad and weak reflections with a d-value of 2.58 nm and 3.07 nm occur before and after ethylene glycolation (Fig. 3b), respectively. The difference between these two values is ~ 0.5 nm, close to the difference between 1.20 nm and 1.72 nm, presumably due to the occurrence of interstratified non-swelling layers (Whitney, 1983). In the present experimental system, the non-swelling layers are probably low-charged saponite which has a talc-like behaviour favored by the low pre-setted charge of saponite (0.3 per half unit cell) (Christidis and Mitsis, 2006; Petit et al., 2008; Fonteneau et al., 2020).

The FTIR spectrum of sample 220-220 (Fig. 4b) only displays the $\nu\text{Mg}_3\text{OH}$ and $\nu\text{Ni}_3\text{OH}$ vibrations at 3675 and 3628 cm^{-1} , respectively. From sample 220-300 to 220-500, with an increase of ΔT , the intensity and resolution of $\nu\text{Mg}_2\text{NiOH}$ and $\nu\text{MgNi}_2\text{OH}$ dramatically increase, and those of $\nu\text{Mg}_3\text{OH}$ and $\nu\text{Ni}_3\text{OH}$ decrease concomitantly (Fig. 4b). In the case of 220-500, the intensities of $\nu\text{Mg}_2\text{NiOH}$ and $\nu\text{MgNi}_2\text{OH}$ are much stronger than those of $\nu\text{Mg}_3\text{OH}$ and $\nu\text{Ni}_3\text{OH}$, indicating a more random distribution of octahedral Mg and Ni.

HAADF-STEM images of the samples in Series II display prominent morphological evolution with increasing ΔT (Fig. 8). Some big particles with a size of ~ 100 nm and small shapeless particles are observed in sample 220-220 (Fig. 8a) and 220-300 (Fig. 8b). The particle size in sample 220-300 seems more uniform than that in sample 220-220. As the hydrothermal temperature increases, the particle size dramatically increases. In sample 220-400, the size of most particles reaches 200 nm in-plane, and there are less small particles overlying in comparison to samples 220-220 and 220-300 (Fig. 8c). For sample 220-500, most particles approach 400 nm in size, and

particles less than 50 nm are scarcely observed (Fig. 8d). In the samples 220-400 and 220-500, euhedral elongated particles occur with high frequency (Fig. 8c and d). Note that the HAADF-STEM images of saponite layers in sample 220-400 show the evidence of micro-phase segregation, with a typical surrounding structure (Fig. 9a) and irregular patchworks of micro-regions (Fig. 9b). In addition, HRTEM images of ultrathin sections of the samples in Series II also provide supplementary information about particle size, as well as dis(order) of layer stacking (Fig. 10). With the increase of hydrothermal temperature (from sample 220-220 to 220-500), saponite layers along *a*- or *b*-axis extend and the order of layer stacking along *c*-axis increases. For example, in sample 220-220, lattice fringe images show most of particles have a length of 50-150 nm and height of 3-10 layers (Fig. 10a), similar to other samples synthesized at 220 °C (e.g., gel-220, 150-220, and 180-220), while for sample 220-500, particles more than 250 nm in length and 6-15 layers in height were observed (Fig. 10d). Such results indicate the prominent increase of particle size with hydrothermal temperature increasing.

DISCUSSION

Crystal-chemistry features of saponite

As shown by FTIR spectra (Fig. 4), the occurrence of $\nu\text{Mg}_2\text{NiOH}$ and $\nu\text{MgNi}_2\text{OH}$ suggests the distribution of Mg and Ni in neighboring octahedral sites in the synthetic saponites, implying dissolution of Mg- and Ni-saponite precursors and recrystallization of Mg-Ni mixed saponite (Zhang et al., 2020). Both the distribution feature of Mg and Ni cations in the Mg,Ni-saponite (i.e., mixing degree of Mg and Ni in octahedral sites) and the dissolution of Mg- and Ni-saponite precursors can be revealed by $R_{(\text{IR})}$ that is usually obtained via decomposition of the structural OH stretching vibrations in FTIR spectra

(Zhang et al., 2020). Figure 11 is an example (sample 220-400) for the spectral deconvolution, and the corresponding $R_{(IR)}$ value (0.44) and estimated dissolution extent (0.59) were obtained by using the method described in Materials and Methods. The calculated $R_{(IR)}$ values for all the synthetic saponites and dissolution extent indexes of the corresponding precursors were summarized in Table 2.

For the synthetic saponites in Series I, the $R_{(IR)}$ values increase with an increase in ΔT , i.e., from ~0.00 for sample 220-220 to 0.63 for sample gel-220. A maximum of $R_{(IR)}$ value, 0.63, was obtained from the sample gel-220, while that of sample 50-220 is 0.60. The $R_{(IR)}$ values of samples gel-220 and 50-220 are close to the theoretical one (0.75) for saponite in which the distribution of Mg and Ni is totally random. The above-mentioned deviations are probably due to the inevitable imprecision of the decomposition (Zhang et al., 2020). Meanwhile, the residual interlayer water may also generate a small band in the region of structural-OH stretching vibration in FTIR spectra of smectite (Johnston, 2017). Thus, it can be inferred that the cation distribution in samples gel-220 and 50-220 is highly random, resulted from the almost complete dissolution of saponite precursors and subsequent recrystallization taking place during the hydrothermal processes. Our calculations show that more than 80% of precursors were dissolved, followed by the recrystallization of Mg,Ni-saponite in samples gel-220 and 50-220 (Table 2). With a decrease of ΔT , the $R_{(IR)}$ value decreases prominently (Table 2) and that of the sample 220-220 almost reaches zero. The low $R_{(IR)}$ values suggest the occurrence of clusters of octahedral Mg and Ni (i.e., Mg- and Ni-domains/layers), instead of a totally random distribution. The occurrence of Mg- and Ni-domains/layers should be attributed to the low dissolution extent of Mg- and Ni-saponite precursors.

Such variations in the distribution of Mg and Ni are also found in the saponites in Series II. For example, the $R_{(IR)}$ of sample 220-500 is 0.58, corresponding to a random distribution of Mg and Ni in the Mg,Ni-saponite. This should be attributed to a high precursors' dissolution extent that is about 0.77 (Table 2). For samples 220-300 and 220-400, partial dissolution of precursors took place during the hydrothermal processes, resulting in a prominent decrease of $R_{(IR)}$. This reflects that the distribution of cations in octahedral sites is less random in comparison to sample 220-500.

Thus, a statistic distribution of cations in the resultant saponites is provided by FTIR spectra. The STEM-EDS analyses provide local information about the cation distribution (Figs. 6 and 7). For example, as shown in Figure 6, the ratios of Mg/Mg+Ni in different locations are fixed at ca. 0.5, showing a relatively homogenous distribution of Mg and Ni within saponite layers/particles. Similar cation distribution is further evidenced by STEM-EDS analyses on a large number of randomly selected particles within the same sample, corresponding to an almost complete dissolution of precursors. The plot for Mg/Mg+Ni ratios of sample 180-220 seems more 'scattered' with more points approaching to 1 or 0 in comparison to those of samples gel-220 and 150-220 (Fig. 7a and b). This suggests that the distribution of Mg and Ni in sample 180-220 is not as homogeneous as that in samples gel-220 and 150-220. The Mg/Mg+Ni value of 1 represent the occurrence of Mg-rich locations while the ratio of 0 correspond to Ni-rich locations within layers/particles. Mg- or Ni-rich locations in the resultant saponite, are possibly due to the undissolved Mg- or Ni-saponite precursor units, respectively.

HAADF-STEM images of the resultant saponites give further evidence for segregations of Mg and Ni cations within one single layer. In the case of 220-400, a

typical surrounding structure within one layer (Fig. 9a) and some layers from the stitched micro-regions (Fig. 9b) are observed. Theoretically, the brighter regions could contain more Ni than the darker ones. According to the FTIR results, the high dissolution extent (0.59) in this sample indicates most of its precursor dissolve. The micro-regions with mixed Mg and Ni (i.e., Mg-Ni mixed saponite) from dissolution-recrystallization are overwhelming, and the relatively small regions could be undissolved precursor units (Mg-saponite or Ni-saponite). Thus, the lighter rim and the darker inner region correspond to Mg-Ni mixed saponite and Mg-saponite, respectively (Fig. 9a). Meanwhile, residual Ni-saponite units attach along the rim of Mg-Ni mixed saponite (Fig. 9b). Here is the most visible evidence for the heterogeneous distribution of Mg and Ni within one layer, resulted from the partial dissolution of precursors and recrystallization and growth of Mg,Ni-saponite. Importantly, such heterogeneity within nano-scale layers offers visual interpretations for the results from FTIR spectra and EDS results.

Crystal growth processes

The morphological evolution of saponites from Series I (Fig. 5) and Series II (Figs. 8 and 10) indicates that the crystal particles of saponites coarsen as long as the hydrothermal temperatures of samples are higher than that of their precursors. In general, the saponite particles from a higher temperature have a larger size compared to those from a lower temperature. In addition, the shapes of crystal size distributions (CSDs) of clay minerals (e.g., smectite, illite/smectite, and illite) are approximately lognormal, and the overall increase of crystal size can result in a right shift of CSD (Eberl et al., 1990; Eberl et al., 1998; Zhang et al., 2020). Hence, we assume the ideal CSDs of saponites synthesized at different temperatures (Fig. 12), in which the dissolution extents are

458 derived from the $R_{(IR)}$ (Table 2) and the critical size is based on the theory of crystal
459 growth (i.e., the hydrothermal system with a higher temperature requiring a larger critical
460 size of particles). When the precursors exposed to a given physicochemical condition, the
461 particles smaller than the critical size would tend to dissolve to decrease the Gibbs free
462 energy of the system (e.g., Kelton, 1991). As shown in Figure 12, for the specific
463 condition of 220 °C, the assumed critical size of saponites is c220. The precursors
464 synthesized at 50 °C completely dissolve when they are hydrothermally treated at 220 °C,
465 suggesting that the particle size of the precursors prepared at 50 °C is smaller than c220.
466 For Series I samples, with the increase of hydrothermal temperature of precursors, the
467 dissolution extents decreases. This indicates that the precursors synthesized at a higher
468 temperature have a lower percentage of particles smaller than the critical size (c220),
469 leading to a lower dissolution (Fig. 12). In Series II, all the samples are synthesized from
470 the same precursors (i.e., a mixture of pMg220 and pNi220) with identical CSD
471 (CSD220). Thus, from sample 220-220 to 220-500, the rise of dissolution extents (i.e.,
472 ~0.00 to 0.77) is related to the subsequent hydrothermal temperatures. The subsequent
473 hydrothermal system with a higher temperature demands a larger critical size of saponites.
474 Thus, with an increase of subsequent temperature, the precursors with CSD220 have a
475 higher percentage of particles smaller than the critical size of the corresponding
476 hydrothermal system. As a result, the higher the subsequent temperature is, the more the
477 precursors with CSD220 dissolve (Fig. 12). Meanwhile, the undissolved particles can
478 grow into stable phases with a larger size and a chemical composition different from that
479 of the initial phase (Steefel and Van Cappellen, 1990).

Saponite growth mechanisms can be determined by its morphological evolution and crystal-chemistry features. For the samples synthesized through a complete dissolution of precursors and recrystallization (e.g., gel-220, 50-220, 220-500), the continuous dissolution of precursors and growth of Mg,Ni-saponite occur during the hydrothermal treatment, in which the species for saponite growth is provided by the dissolution of precursors. However, it is very hard to define the specific growth patterns in such processes due to the lack of kinetic data. Note that the occurrence of non-expandable layers in the case of 220-500 may be due to the super-high temperature (500 °C) of the hydrothermal system (Whitney, 1983). For other samples (e.g., 150-220, 180-220, 200-220, 220-300, and 220-400), their corresponding precursors partially dissolve, depending on ΔT . Thus, the species for saponite growth include the dissolved precursors (i.e., simple chemical species or ions) and residual precursors (i.e., solid saponite nanoparticles). Correspondingly, the growth mechanisms may involve the traditional nucleation-growth pathway and particle attachment. Such an assumption is supported by the previous study about the growth kinetics of saponite (Zhang et al., 2020) and the HAADF-STEM observations in the present study.

The kinetic growth process demonstrated that the saponite layers grow with the dissolution of small-size saponite layers (Zhang et al., 2020). The growth rate of Mg,Ni-saponite could be limited by the concentration of growth species on the edges of particles. In such systems, surface free energy tends toward a minimum by the dissolution of small layers and the growth of large layers as the matter is transferred from the former to the latter through the solution. As a result, the small particles gradually disappear, and the mean crystallite size increases (Lifshitz and Slyozov, 1961; Wagner, 1961). In addition to

the traditional growth pattern, i.e., the dissolution of small layers and the growth of large layers, the attachment of saponite nanoparticles was also involved in the growth pathway to reduce the free energy of the system based on numerous studies about other minerals (De Yoreo et al., 2015). Several clues support the existence of nanoparticle attachment during the kinetic growth process. For example, in sample 150-220, the rate of $R_{(IR)}$ slightly rises, but the mean particle size dramatically increases from 3 to 14 days, suggesting saponite growth accompanied by particle attachment (Zhang et al., 2020). Another very important feature, micro-phase segregation, was found in the resultant saponite (Fig. 9), which confirms the simultaneous occurrence of dissolution-recrystallization pathway and crystallization of particle attachment. Sample 220-400 is a typical example with a dissolution extent of its precursors of 0.59 (Table 2), implying that the dissolution-recrystallization pathway should be the dominant growth mechanism. These micro-phase distributions within one layer indicate the co-existence of Mg-, Ni- and Mg-Ni mixed domains, probably resulting from layer attachment. Thus, for all saponites synthesized through partial dissolution and recrystallization of precursors, their growth processes may accompany with layer attachment.

Evolutionary features of saponite and controlling factors

The changes in temperature will significantly affect the solubility of saponite, pH and chemistry of solution, which could lead to the evolutions of compositions and morphology of saponite. In nature, smectites are stable or metastable over geological time in an unchanged environment but will be destabilized due to the changes in physicochemical conditions (e.g., chemistry, temperature, pressure, etc.). Changes running into smectite's environment would bring about the compositional variability and

crystal growth of smectite. Records of these changes could provide a useful framework for interpreting the geochemistry and long-term stability of clay minerals (Tardy et al., 1987). Present experiments were conducted in a sealed hydrothermal system at different temperatures. Dissolution and recrystallization are the principal driving forces for all re-equilibration reactions in the presence of a fluid phase (Putnis, 2009). Thus, when the saponite precursors that form at a lower temperature are exposed to a higher temperature fluid, solid-solution reactions tend to take place to reduce the free energy of the whole system. The neoformed saponite particles are the products of re-equilibration reactions of the hydrothermal system.

In addition to the change of physicochemical conditions, the presence of kinetic factors (e.g., reaction time, size driven force) may contribute to the smectite evolution. $R_{(IR)}$ in Series I and II have been expressed in terms of the variations of temperature and pressure of hydrothermal systems (Table 2, Fig. 13). Interestingly, $R_{(IR)}$ is probably not only affected by the changes in physicochemical conditions. For instance, sample 220-300 ($\Delta T=80$ °C) necessitates much higher activation energy than sample 150-220 ($\Delta T=70$ °C) during the hydrothermal processes. In contrast, the former case has a lower $R_{(IR)}$ (0.24) than that (0.55) of the latter. In comparison to the samples in Series II, the samples in Series I have a smaller particle size of starting materials and longer reaction time so that the kinetic factors contribute more to the dissolution degree. As nano-scale minerals, the particle size is a key point in determining the energetics and stability of smectite. The smaller particles with higher surface energy correspond to a higher reactivity and lower stability as observed for other nano-scale minerals like Fe(III)-[oxi(hydr)] oxide minerals (Anschutz and Penn, 2005; Madden and Hochella 2005; Hochella et al., 2008; Navrotsky

et al., 2008). Therefore, the size driving force may induce the evolution of smectite, even if there is no change of physicochemical conditions.

IMPLICATIONS

Our study indicates that the distribution mode of octahedral cations in saponite is not only relevant to a given hydrothermal temperature but also dependent on ΔT for final products. In nature, large Ni clusters were systematically observed in natural (Ni-Mg)-phyllosilicates formed at a low temperature in lateritic weathering profiles (Gérard and Herbillon, 1983; Manceau and Calas, 1985; Decarreau et al., 1987). During the synthesis of clay minerals, when the temperature of synthesis decreases, a tendency to clustering was also observed and specially marked for Ni atoms (Decarreau et al., 1992). These previous results indicated that segregation is frequently observed in clay minerals formed at low temperatures, thereby the distribution type could be temperature-dependent. However, our experiments give information that the element distributions within clay minerals are also related to the synthesis temperature gap between starting materials and resultant products. Larger Mg- or Ni- clusters can form when the respective synthesis temperatures of the starting materials and the resultant products are close (i.e., low ΔT). Thus, the clustering is not only related to given temperature conditions but also to the characteristics of the starting materials in terms of crystallinity and particle size. Consequently, the distribution mode of octahedral cations in saponite can not be used as a geothermometer. Such results also indicate the various isomorphous substitutions or solid solutions in natural clay minerals are probably related to the properties of raw materials.

Weathering may yield clay minerals with poor crystalline and small particles, which could transport into sedimentary environments (Wilson and Jones, 1983; Galán

and Ferrell, 2013). Clay minerals deposited in a sedimentary environment (e.g., subsiding basin) are buried, heated, and eventually enter diagenetic-hydrothermal environments (Eberl, 1984; Merriman, 2005). As the environment changes, the most important reactions are phase transformation and crystal growth, accompanied by cation redistribution. Crystal-chemistry and crystal growth could be used to predict the environmental transition and element migration. The experimental system used here was very simple compared to natural systems that are far much complex. However, it was possible to describe smectite evolution by element redistribution and growth. In nature, such evolutions of clay minerals are difficult to capture in the early geological stage. Similar experiments with more complexities could offer potentials to predict the mineral geochemistry and better understand and parametrize natural processes.

ACKNOWLEDGMENT

The authors acknowledge A. Decarreau for the discussions that enriched this paper. The financial supports of National Natural Science Foundation of China (Grant Nos. 41921003, 41530313, 41772039), National Science Fund for Distinguished Young Scholars of China (Grant No.41825003), Key Research Program of Frontier Sciences, CAS (Grant No. QYZDJ-SSW-DQC023), the European Union (ERDF), "Région Nouvelle Aquitaine," French « Ministère de l'Enseignement Supérieur et de la Recherche », and China Scholarship Council are much appreciated.

REFERENCES

Anschutz, A.J., and Penn, R.L. (2005) Reduction of crystalline iron (III) oxyhydroxides using hydroquinone: Influence of phase and particle size. *Geochemical Transactions*, 6(3), 60.

- 594 Baldermann, A., Warr, L.N., Letofskypapst, I., and Mavromatis, V. (2015) Substantial iron sequestration
595 during green-clay authigenesis in modern deep-sea sediments. *Nature Geoscience*, 8(11), 885-889.
- 596 Banfield, J.F., and Eggleton, R.A. (1990) Analytical transmission electron microscope studies of
597 plagioclase, muscovite, and K-feldspar weathering. *Clays and Clay Minerals*, 38(1), 77-89.
- 598 Brigatti, M.F., Galan, E., and Theng, B.K.G. (2006) Chapter 2 - Structures and Mineralogy of Clay
599 Minerals. In F. Bergaya, B.K.G. Theng, and G. Lagaly, Eds. *Developments in Clay Science*, 1, p.
600 19-86. Elsevier.
- 601 Brindley, G. (1966) Ethylene glycol and glycerol complexes of smectites and vermiculites. *Clay Minerals*,
602 6(4), 237-259.
- 603 Borchardt, G. (1989) Chapter 14 - Smectites. In J.B. Dixon and S.B. Weed, Eds. *Minerals in soil*
604 environments, 1, p. 675-727. Wiley.
- 605 Cuadros, J., Andrade, G.R.P., Ferreira, T.O., Partiti, C.S.D.M., Cohen, R., and Vidaltorradó, P. (2017) The
606 mangrove reactor: fast clay transformation and potassium sink. *Applied Clay Science*, 140, 50-58.
- 607 Christidis, G.E. (2001) Formation and growth of smectites in bentonites: a case study from Kimolos Island,
608 Aegean, Greece. *Clays and Clay Minerals*, 49(3), 204-215.
- 609 Christidis, G.E., and Huff, W.D. (2009) Geological aspects and genesis of bentonites. *Elements*, 5(2), 93-
610 98.
- 611 Christidis, G.E., and Mitsis, I. (2006) A new Ni-rich stevensite from the ophiolite complex of Othrys,
612 Central Greece. *Clays and Clay Minerals*, 54(6), 653-666.
- 613 De Yoreo, J.J., Gilbert, P.U., Sommerdijk, N.A., Penn, R.L., Whitlam, S., Joester, D., Zhang, H., Rimer,
614 J.D., Navrotsky, A., and Banfield, J.F. (2015) Crystallization by particle attachment in synthetic,
615 biogenic, and geologic environments. *Science*, 349(6247), aaa6760.
- 616 Decarreau, A., Colin, F., Herbillon, A., Manceau, A., Nahon, D., Paquet, H., Trauth-Badaud, D., and
617 Trescases, J. (1987) Domain segregation in Ni-Fe-Mg-smectites. *Clays and Clay Minerals*, 35(1),
618 1-10.
- 619 Decarreau, A., Grauby, O., and Petit, S. (1992) The actual distribution of octahedral cations in 2: 1 clay
620 minerals: results from clay synthesis. *Applied Clay Science*, 7(1-3), 147-167.

- 621 Decarreau, A., Petit, S., Martin, F., Farges, F., Vieillard, P., and Joussein, E. (2008) Hydrothermal
622 synthesis, between 75 and 150 °C, of high-charge, ferric nontronites. *Clays and Clay Minerals*,
623 56(3), 322-337.
- 624 Eberl, D. (1984) Clay mineral formation and transformation in rocks and soils. *Philosophical Transactions*
625 of the Royal Society of London. Series A, Mathematical and Physical Sciences, 311(1517), 241-
626 257.
- 627 Eberl, D., Drits, V., and Środoń, J. (1998) Deducing growth mechanisms for minerals from the shapes of
628 crystal size distributions. *American journal of Science*, 298(6), 499-533.
- 629 Eberl, D., Środoń, J., Kralik, M., Taylor, B.E., and Peterman, Z.E. (1990) Ostwald ripening of clays and
630 metamorphic minerals. *Science*, 248(4954), 474-477.
- 631 Fonteneau, L., Caner, L., Petit, S., Juillot, F., Ploquin, F., and Fritsch, E. (2020) Swelling capacity of mixed
632 talc-like/stevensite layers in white/green clay infillings ('deweylite'/'garnierite') from serpentine
633 veins of faulted peridotites, New Caledonia. *American Mineralogist*, in press.
- 634 Galán, E., and Ferrell, R.E. (2013) Chapter 3 - Genesis of Clay Minerals. In F. Bergaya, and G. Lagaly,
635 Eds. *Developments in Clay Science*, 5, p. 83-126. Elsevier.
- 636 Gérard, P., and Herbillon, A. (1983) Infrared studies of Ni-bearing clay minerals of the kerolite-pimelite
637 series. *Clays and Clay Minerals*, 31(2), 143-151.
- 638 Hazen, R.M., Sverjensky, D.A., Azzolini, D., Bish, D.L., Elmore, S.C., Hinnov, L., and Milliken, R.E.
639 (2013) Clay mineral evolution. *American Mineralogist*, 98(11-12), 2007-2029.
- 640 He, H., Li, T., Tao, Q., Chen, T., Zhang, D., Zhu, J., Yuan, P., and Zhu, R. (2014) Aluminum ion
641 occupancy in the structure of synthetic saponites: Effect on crystallinity. *American Mineralogist*,
642 99(1), 109-116.
- 643 Hochella, M.F., Lower, S.K., Maurice, P.A., Penn, R.L., Sahai, N., Sparks, D.L., and Twining, B.S. (2008)
644 Nanominerals, mineral nanoparticles, and earth systems. *Science*, 319(5870), 1631-1635.
- 645 Johnston, C.T. (2017) Chapter 9 - Infrared Studies of Clay Mineral-Water Interactions. In W.P. Gates, J.T.
646 Klopogge, J. Madejová, and F. Bergaya, Eds. *Developments in Clay Science*, 8, p. 288-309.
647 Elsevier.

- 648 Kawano, M., and Tomita, K. (1992) Formation of allophane and beidellite during hydrothermal alteration
649 of volcanic glass below 200 oC. *Clays and Clay Minerals*, 40(6), 666-674.
- 650 Kelton, K.F. (1991) Crystal Nucleation in Liquids and Glasses. In H. Ehrenreich, and D. Turnbull, Eds.
651 Solid State Physics, 45, p. 75-177. Academic Press.
- 652 Klopogge, J.T., Komarneni, S., and Amonette, J.E. (1999) Synthesis of smectite clay minerals: a critical
653 review. *Clays and Clay Minerals*, 47(5), 529-554.
- 654 Lifshitz, I.M., and Slyozov, V.V. (1961) The kinetics of precipitation from supersaturated solid solutions.
655 *Journal of physics and chemistry of solids*, 19(1-2), 35-50.
- 656 Madden, A.S., and Hochella, M.F. (2005) A test of geochemical reactivity as a function of mineral size:
657 Manganese oxidation promoted by hematite nanoparticles. *Geochimica et Cosmochimica Acta*,
658 69(2), 389-398.
- 659 Madejová, J., Gates, W.P., and Petit, S. (2017) Chapter 5 - IR Spectra of Clay Minerals. In W.P. Gates, J.T.
660 Klopogge, J. Madejová, and F. Bergaya, Eds. *Developments in Clay Science*, 8, p. 107-149.
661 Elsevier.
- 662 Manceau, A., and Calas, G. (1985) Heterogeneous distribution of nickel in hydrous silicates from New
663 Caledonia ore deposits. *American Mineralogist*, 70(5-6), 549-558.
- 664 Merriman, R.J. (2005) Clay minerals and sedimentary basin history. *European Journal of Mineralogy*,
665 17(1), 7-20.
- 666 Navrotsky, A., Mazeina, L., and Majzlan, J. (2008) Size-driven structural and thermodynamic complexity
667 in iron oxides. *Science*, 319(5870), 1635-1638.
- 668 Petit, S., Baron, F., and Decarreau, A. (2017) Synthesis of nontronite and other Fe-rich smectites: a critical
669 review. *Clay Minerals*, 52(4), 469-483.
- 670 Petit, S., and Madejová, J. (2013) Chapter 2.7 - Fourier Transform Infrared Spectroscopy. In F. Bergaya,
671 and G. Lagaly, Eds. *Developments in Clay Science*, 5, p. 213-231. Elsevier.
- 672 Petit, S., Martin, F., Wiewiora, A., De Parseval, P., and Decarreau, A. (2004) Crystal-chemistry of talc: A
673 near infrared (NIR) spectroscopy study. *American Mineralogist*, 89(2-3), 319-326.
- 674 Petit, S., Righi, D., and Decarreau, A. (2008) Transformation of synthetic Zn-stevensite to Zn-talc induced
675 by the Hofmann-Klemen effect. *Clays and Clay Minerals*, 56(6), 645-654.

- 676 Putnis, A. (2009) Mineral replacement reactions. Reviews in mineralogy and geochemistry, 70(1), 87-124.
- 677 Slonimskaya, M., Besson, G., Dainyak, L., Tchoubar, C., and Drits, V. (1986) Interpretation of the IR
678 spectra of celadonites and glauconites in the region of OH-stretching frequencies. Clay Minerals,
679 21(3), 377-388.
- 680 Steefel, C.I., and Van Cappellen, P. (1990) A new kinetic approach to modeling water-rock interaction: The
681 role of nucleation, precursors, and Ostwald ripening. Geochimica et Cosmochimica Acta, 54(10),
682 2657-2677.
- 683 Suquet, H., Malard, C., Copin, E., and Pezerat, H. (1981) Variation du paramètre b et de la distance basale
684 d 001 dans une série de saponites à charge croissante: I. Etats hydratés. Clay Minerals, 16(1), 53-
685 67.
- 686 Tardy, Y., Duplay, J., and Fritz, B. (1987) Stability fields of smectites and illites as a function of
687 temperature and chemical composition. Swedish Nuclear Fuel and Waste Management Co, p. 3-8.
- 688 Voigt, M., Pearce, C.R., Fries, D.M., Baldermann, A., and Oelkers, E.H. (2020) Magnesium isotope
689 fractionation during hydrothermal seawater-basalt interaction. Geochimica et Cosmochimica Acta,
690 272, 21-35.
- 691 Wagner, C. (1961) Theorie der alterung von niederschlägen durch umlösen (Ostwald-reifung). Zeitschrift
692 für Elektrochemie, Berichte der Bunsengesellschaft für physikalische Chemie, 65(7-8), 581-591.
- 693 Whitney, G. (1983) Hydrothermal reactivity of saponite. Clays and Clay Minerals, 31(1), 1-8.
- 694 Wilson, M., and Jones, D. (1983) Lichen weathering of minerals: implications for pedogenesis. Geological
695 Society, London, Special Publications, 11(1), 5-12.
- 696 Zhang, C., Petit, S., He, H., Villiéras, F., Razafitianamaharavo, A., Baron, F., Tao, Q., and Zhu, J. (2020)
697 Crystal Growth of Smectite: A Study Based on the Change in Crystal Chemistry and Morphology
698 of Saponites with Synthesis Time. ACS Earth and Space Chemistry, 4(1), 14-23.
- 699 Zhang, D., Zhou, C. H., Lin, C. X., Tong, D. S., and Yu, W. H. (2010) Synthesis of clay minerals. Applied
700 Clay Science, 50(1), 1-11.
- 701 Zhou, Z., and Fyfe, W. (1989) Palagonitization of basaltic glass from DSDP Site 335, Leg 37; textures,
702 chemical composition, and mechanism of formation. American Mineralogist, 74(9-10), 1045-
703 1053.

704

705

FIGURE CAPTIONS

706 **Figure 1.** Powder XRD patterns of Mg-saponite (a) and Ni-saponite (b) precursors

707 synthesized at different temperatures for one day.

708 **Figure 2.** Structural OH stretching vibration region in the FTIR spectra of Mg-saponite (a)

709 and Ni-saponite (b) precursors synthesized at different temperatures for one day.

710 **Figure 3.** XRD patterns of oriented samples (air-dried - red dot; after glycolation - black

711 solid). a, Series I. b, Series II.

712 **Figure 4.** The Structural OH stretching vibration region of the FTIR spectra of synthetic

713 samples. a, Series I. b, Series II.

714 **Figure 5.** HRTEM images of Mg- and Ni-saponite precursors (a, b, d, e, g, h) and the

715 corresponding synthetic Mg,Ni-saponites from Series I (c, f, i).

716 **Figure 6.** The (Mg/Mg+Ni) ratios deduced from STEM-EDS analyses at different

717 positions along a single particle in a ultra-thin section.

718 **Figure 7.** The Mg/(Mg+Ni) ratios for saponites prepared from different precursors. a,

719 gel-220. b, 150-220. c, 180-220. For each sample, the squares with the same color

720 connected by a dotted line correspond to the Mg/(Mg+Ni) ratios at different positions

721 within the same particle.

722 **Figure 8.** STEM images of synthetic saponites in Series II. a, 220-220. b, 220-300. c,

723 220-400. d, 220-500.

Figure 9. HAADF-STEM images of saponite layers from sample 220-400, the darker areas could be Mg-rich while the lighter ones could be Ni-rich.

Figure 10. HRTEM images of synthetic saponites in Series II. a, 220-220. b, 220-300. c, 220-400. d, 220-500.

Figure 11. Decomposition and fitting of the ν OH vibrations in the FTIR spectrum of sample 200-400.

Figure 12. The assumed CSDs of synthesized saponite under different physicochemical conditions. Series I, the red areas are the dissolution extents of precursors synthesized at different temperature (50, 150, 180, and 220 °C) after subsequent hydrothermal treatment at 220 °C; Series II, the red area, is the dissolution extents of precursors synthesized at 220 °C after exposing to the different hydrothermal systems (220, 300, 400, and 500 °C). cT stands for the required critical size in corresponding physicochemical system, e.g., c220 is the critical size of saponite in the hydrothermal system at 220 °C.

Figure 13. Temperature and pressure diagram in closed hydrothermal systems. Percentages denote the $R_{(IR)}$ of saponite from one physicochemical condition to another one. Red, series I. Blue, series II.

TABLES

Table 1. The synthesis conditions of hydrothermal products at 220, 300, 400 and 500 °C.

	Samples	precursors	Temperature (°C)		Pressure (Mpa)		pH _i	pH _f
			precursors	products	precursors	products		
Series I	gel-220	PMg-gel; pNi-gel	RT	220	--	2.5	10.20	9.59
	50-220	pMg50; pNi50	50	200	0.1	2.5	10.16	9.56
	150-220	pMg150; pNi150	150	220	1.0	2.5	10.02	9.57
	180-220	pMg180; pNi180	180	220	1.6	2.5	9.95	10.17
	200-220	pMg200; pNi200	200	220	2.0	2.5	9.54	9.52
	220-220	pMg220; pNi220	220	220	2.5	2.5	8.59	8.98
Series II	220-220	pMg220; pNi220	220	220	2.5	2.5	8.59	8.87
	220-300	pMg220; pNi220	220	300	2.5	7.5	8.59	7.90
	220-400	pMg220; pNi220	220	400	2.5	61.0	8.59	7.86
	220-500	pMg220; pNi220	220	500	2.5	136.0	8.59	7.40

Table 2. $R_{(IR)}$ for all synthetic Mg,Ni-saponites and calculated dissolution extents for the corresponding precursors.

	Samples	$R_{(IR)}$	Dissolution extent	ΔT (°C)
Series I	Gel-220	0.63	0.84	~200
	50-220	0.60	0.80	170
	150-220	0.55	0.73	70
	180-220	0.30	0.40	40
	200-220	0.17	0.23	20
	220-220	~0.00	~0.00	0
Series II	220-220	~0.00	~0.00	0
	220-300	0.24	0.32	80
	220-400	0.44	0.59	180
	220-500	0.58	0.77	280

Figure 1

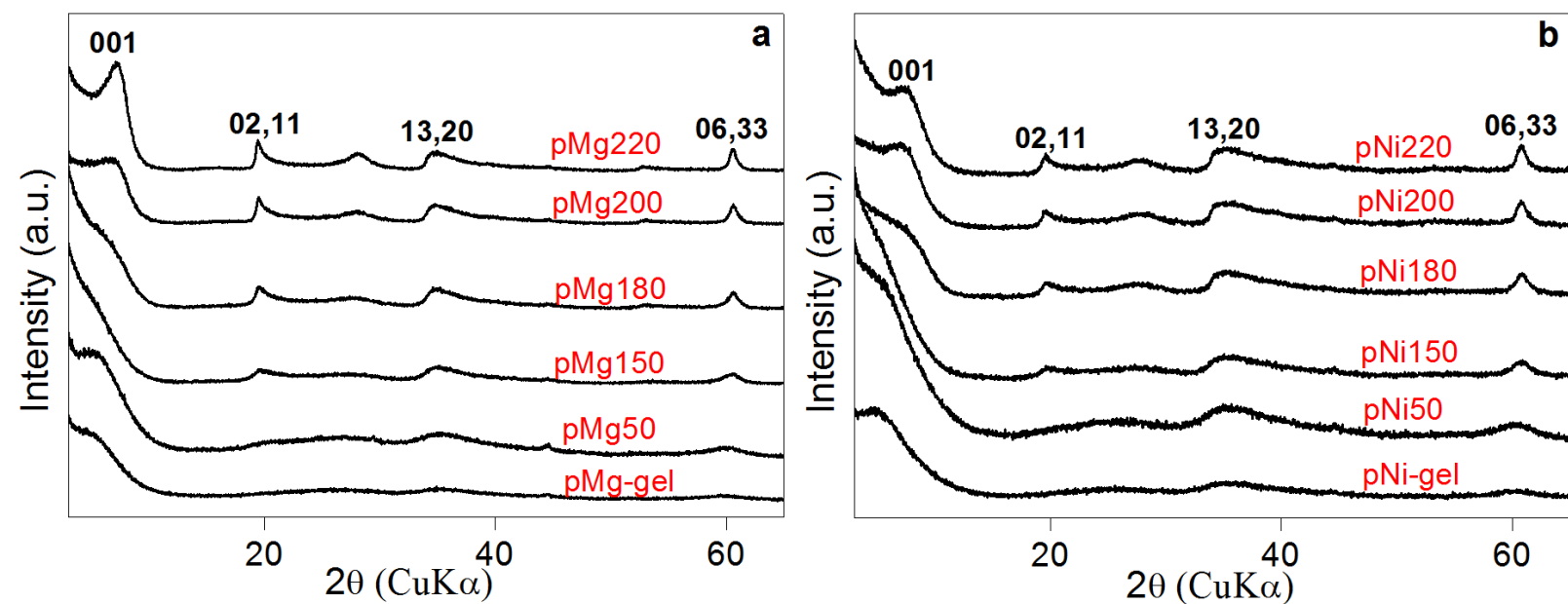


Figure 2

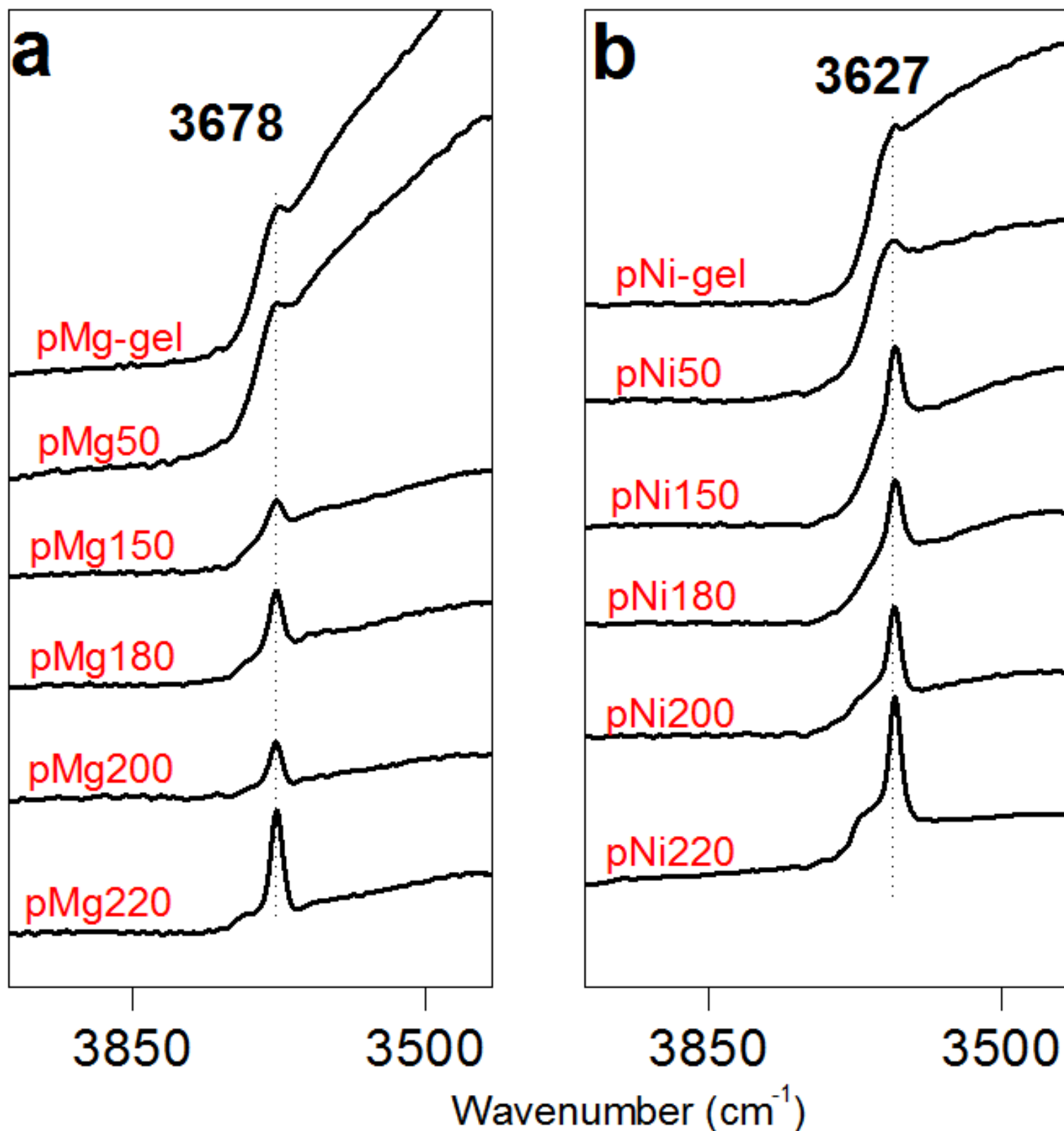


Figure 3

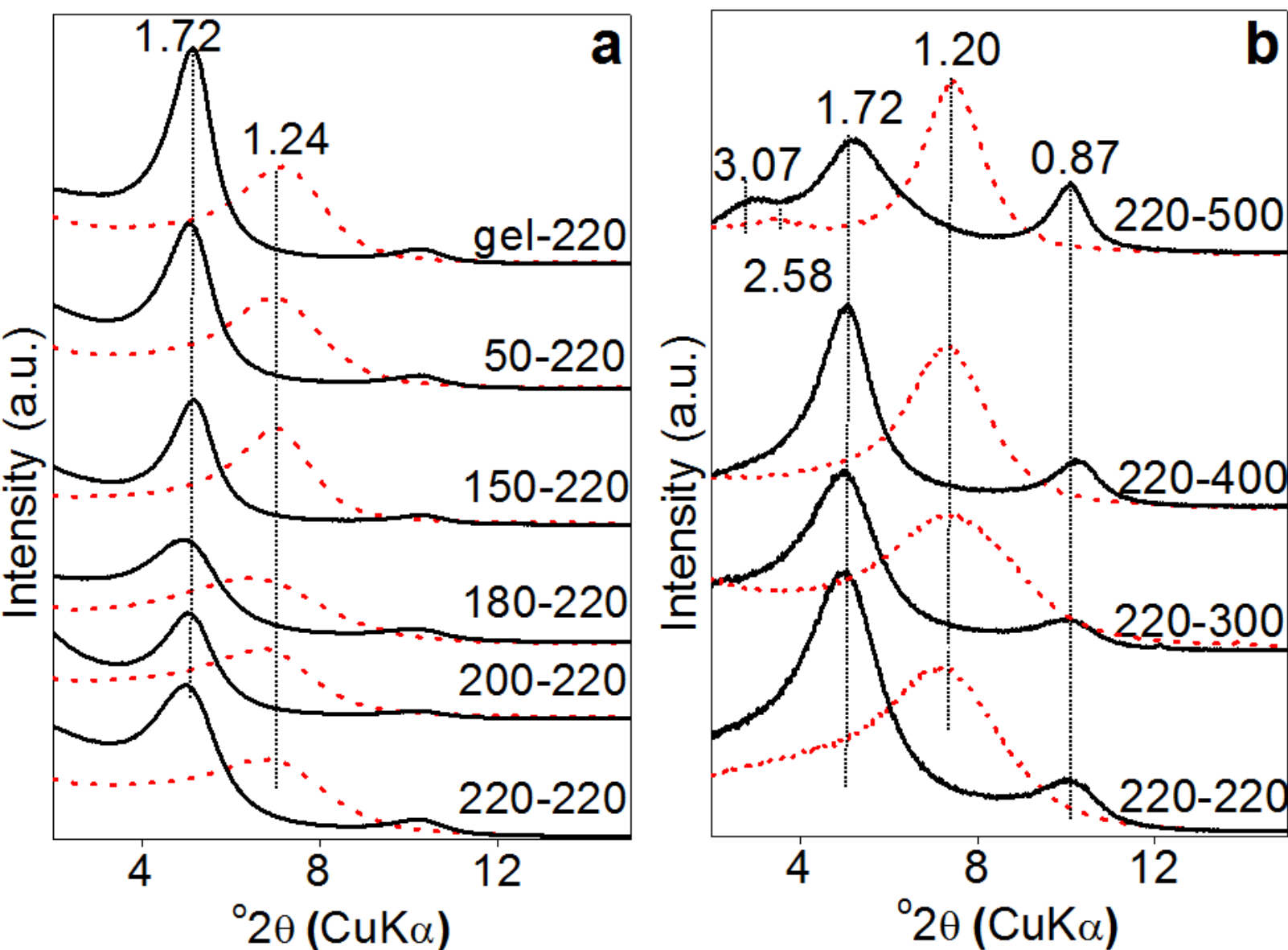


Figure 4

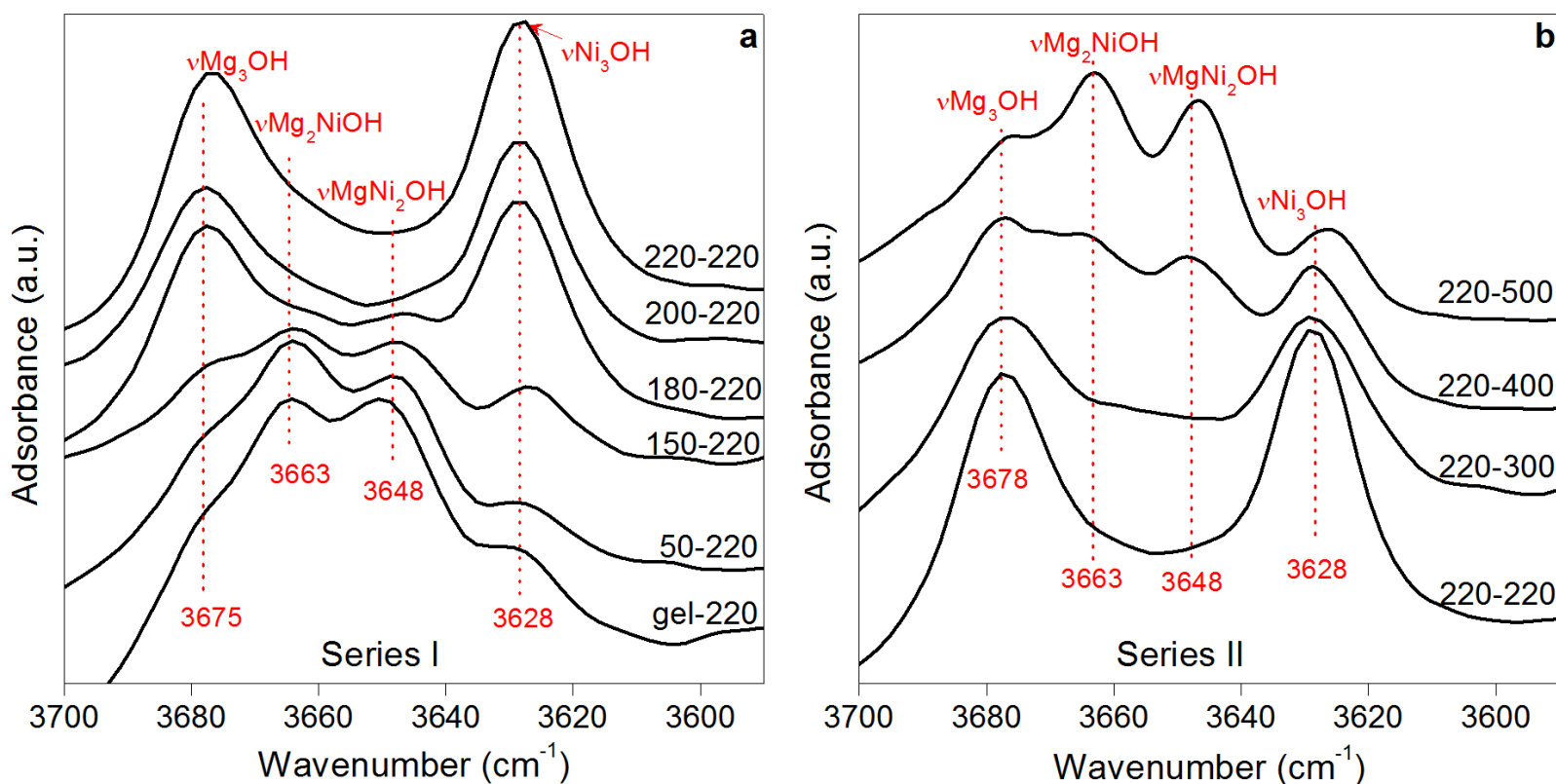


Figure 5

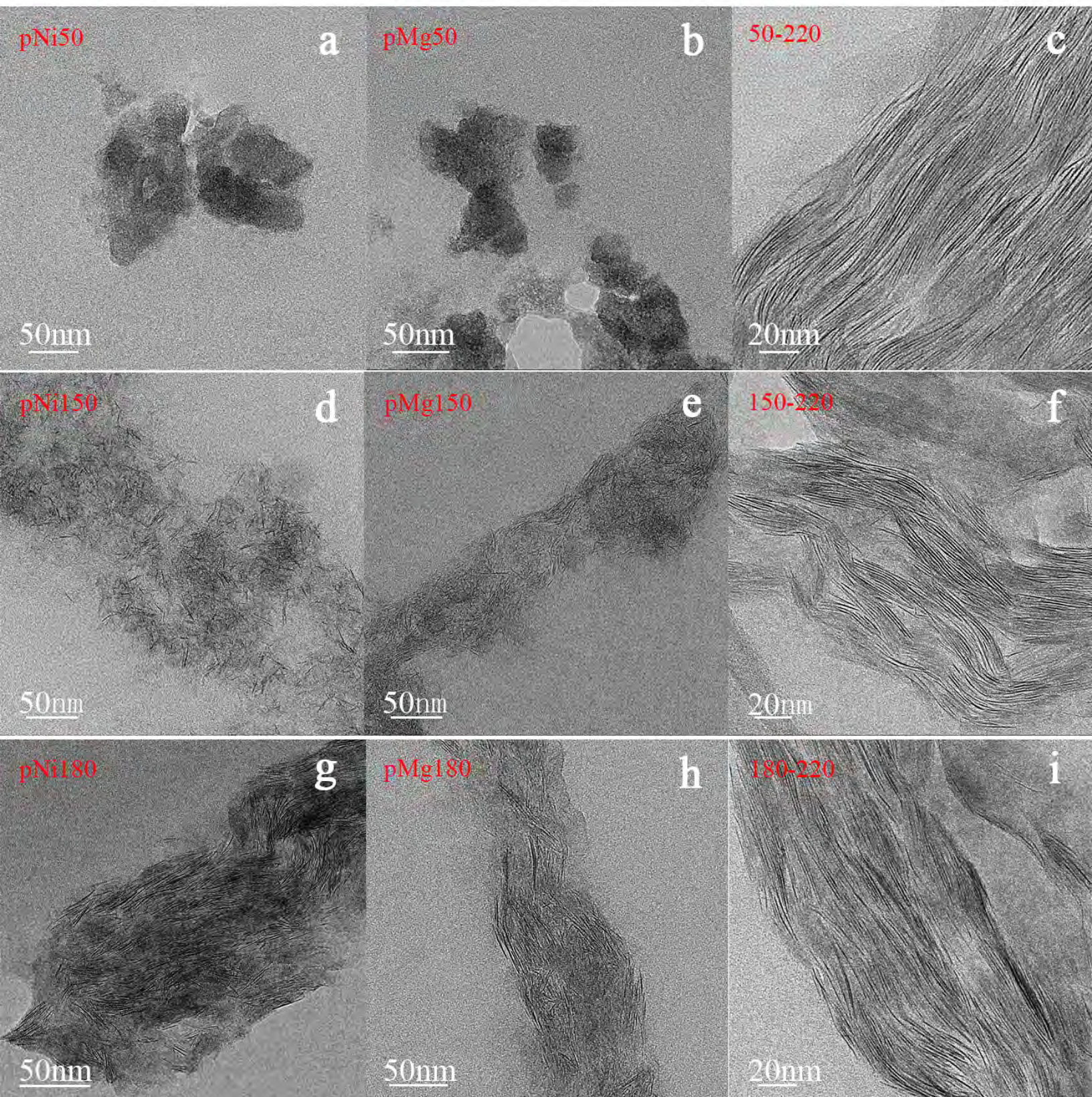
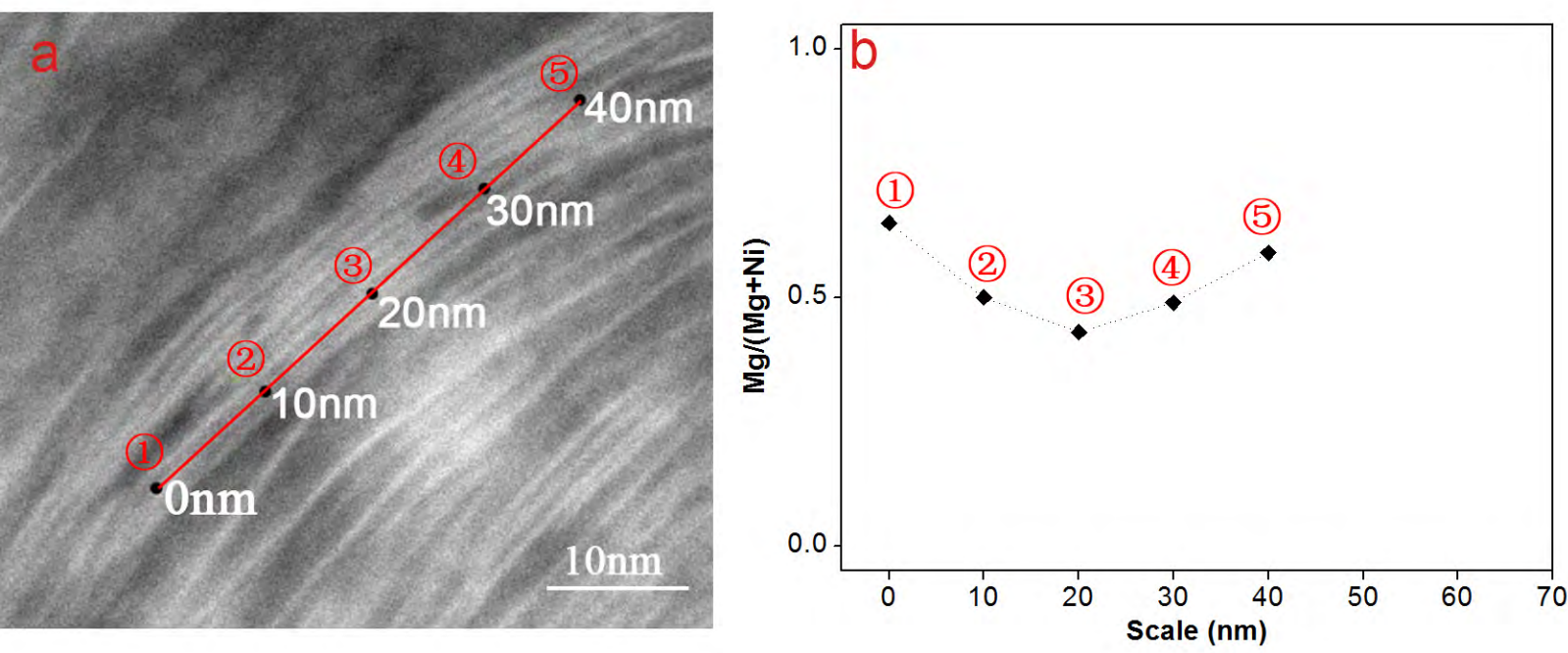


Figure 6



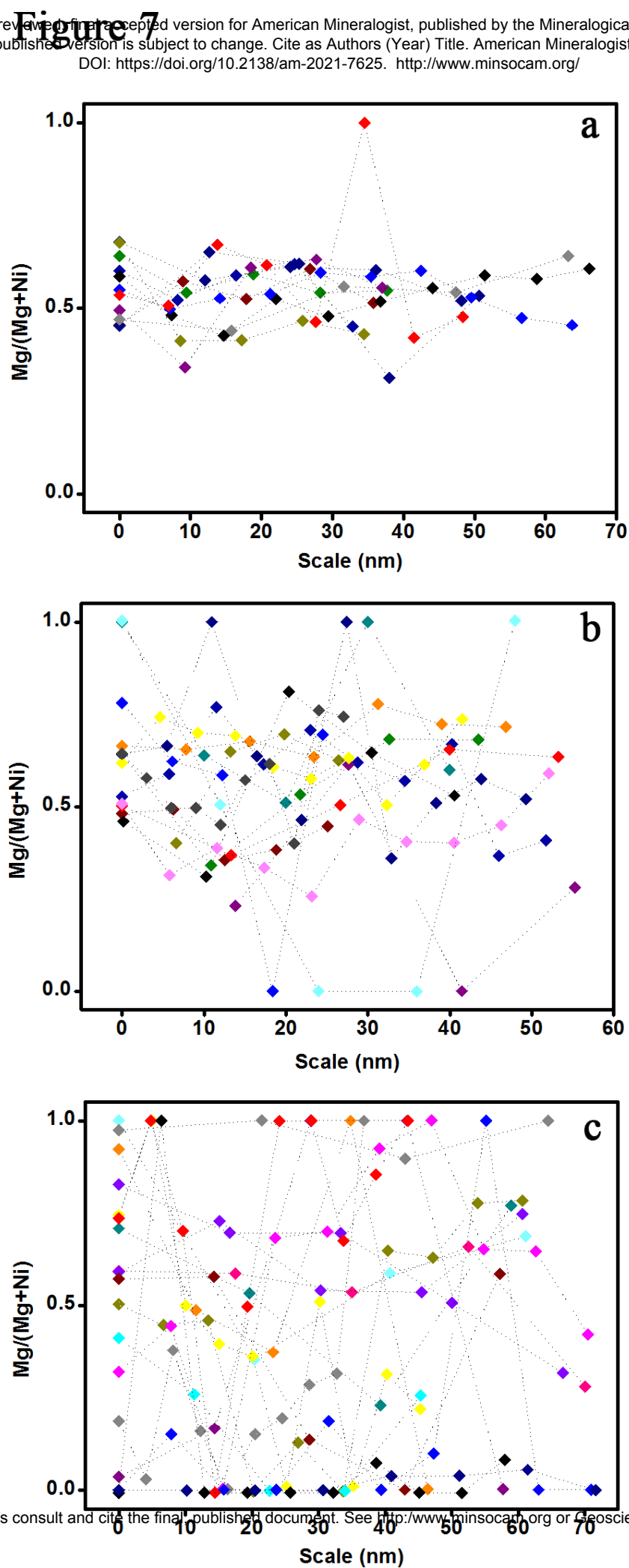


Figure 8

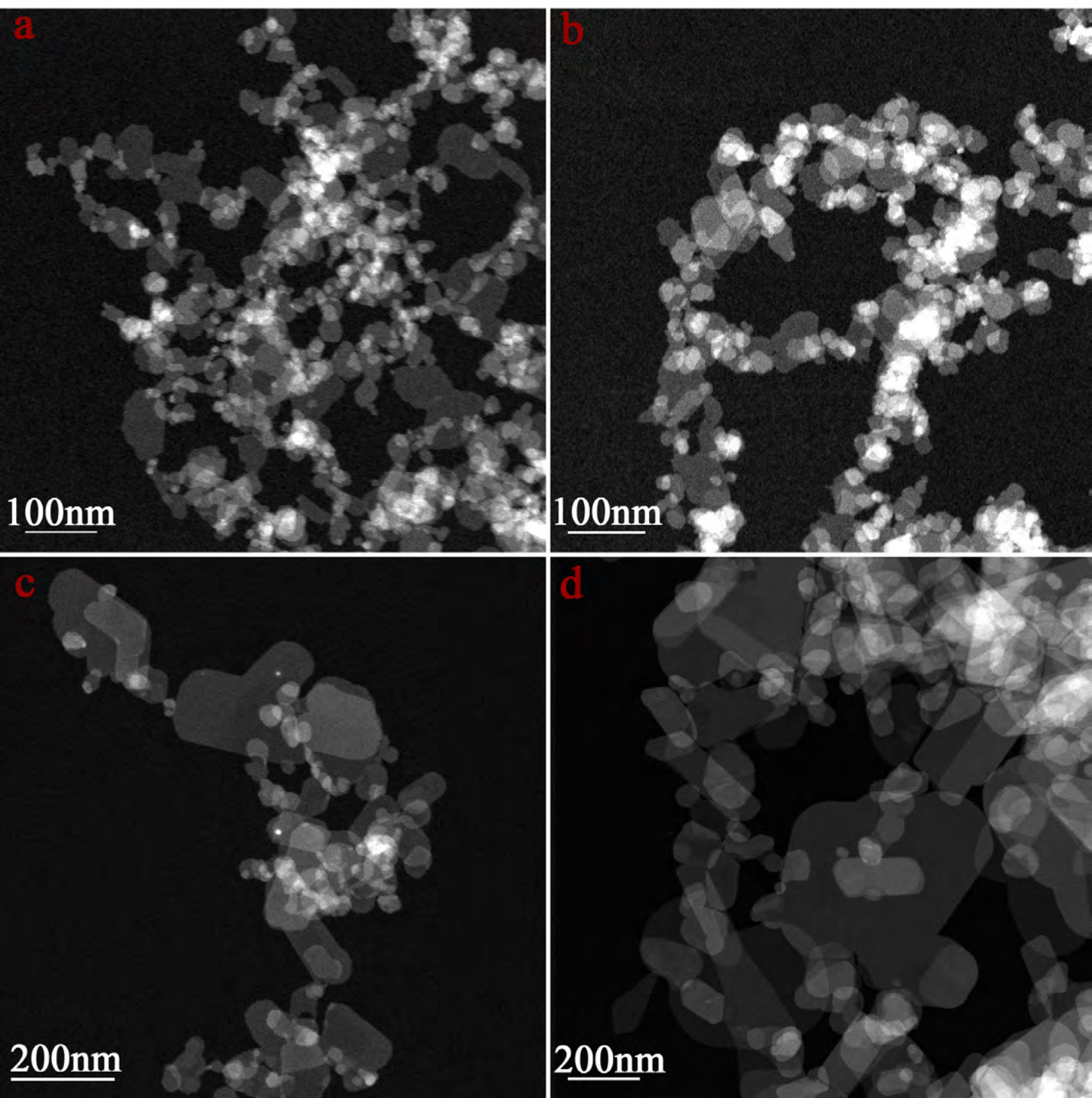


Figure 9

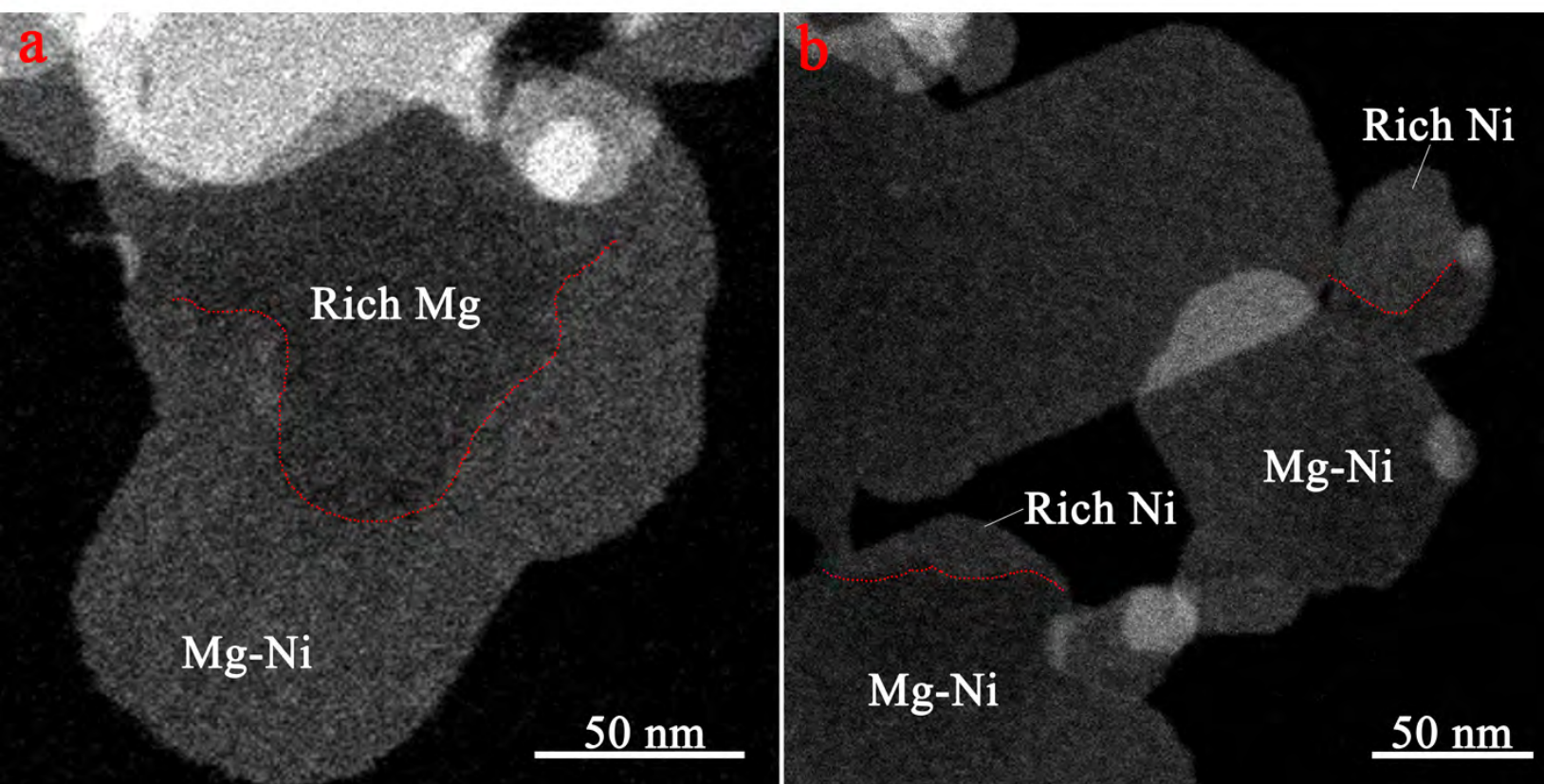


Figure 10

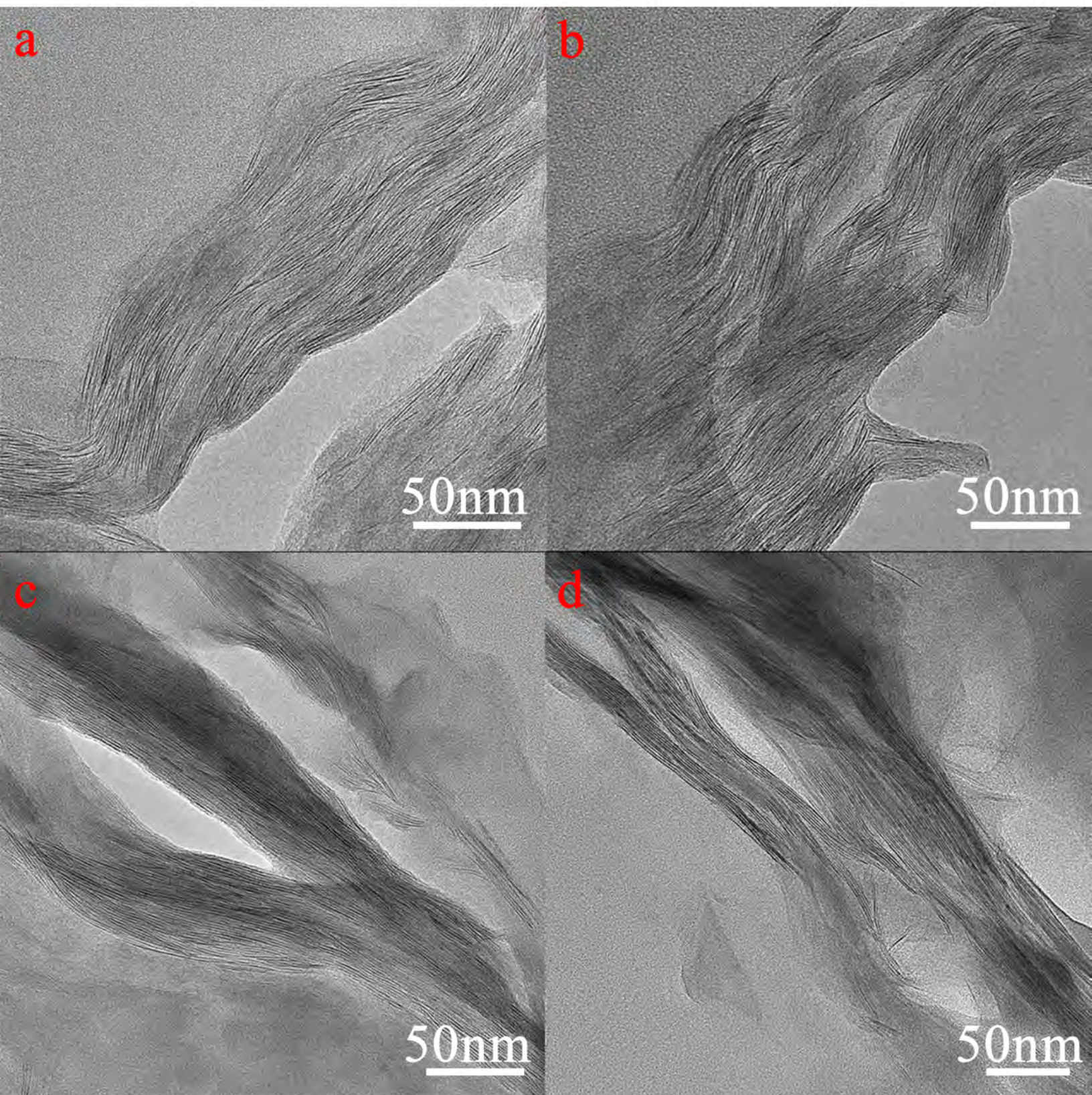


Figure 11

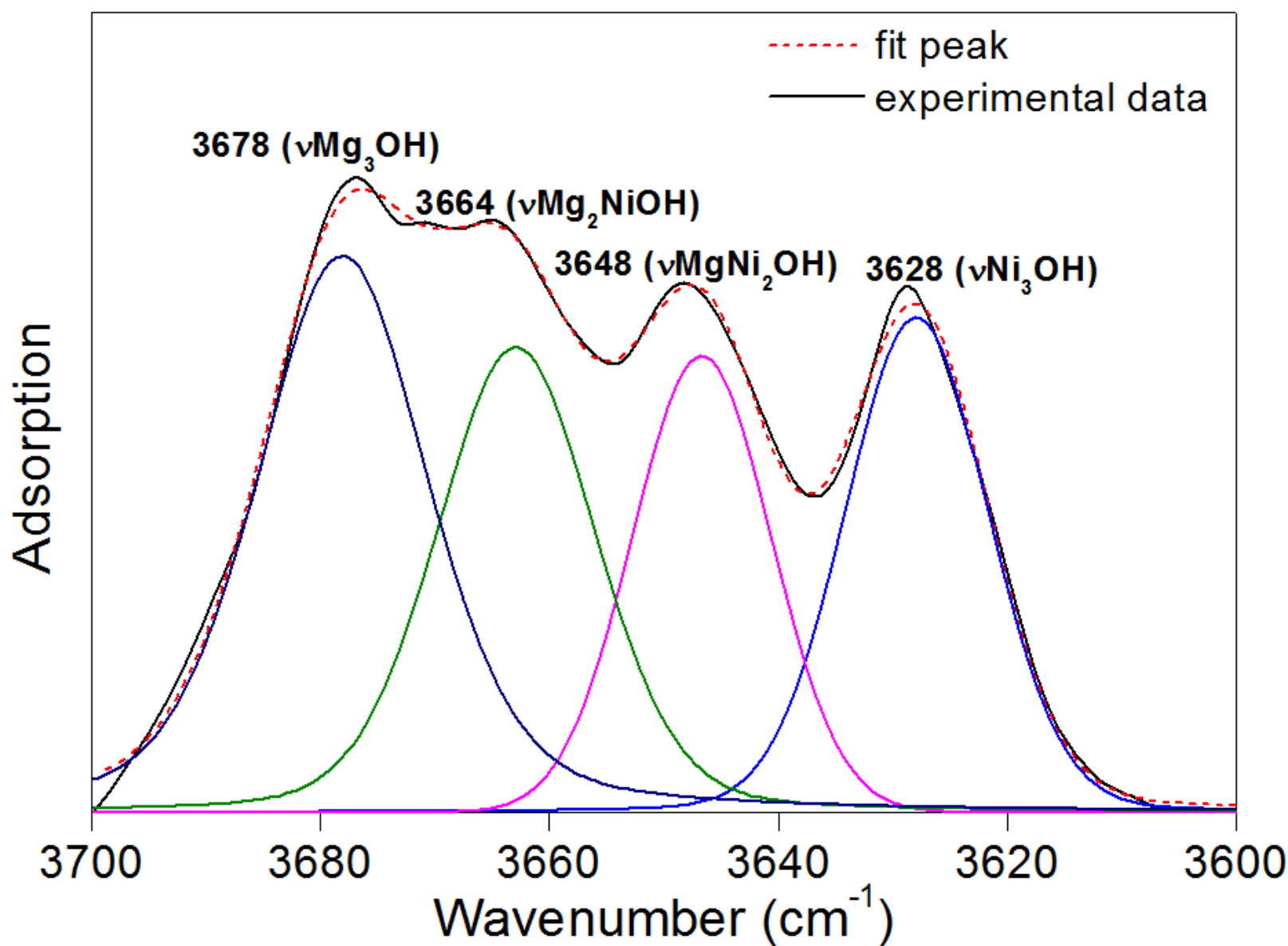


Figure 12

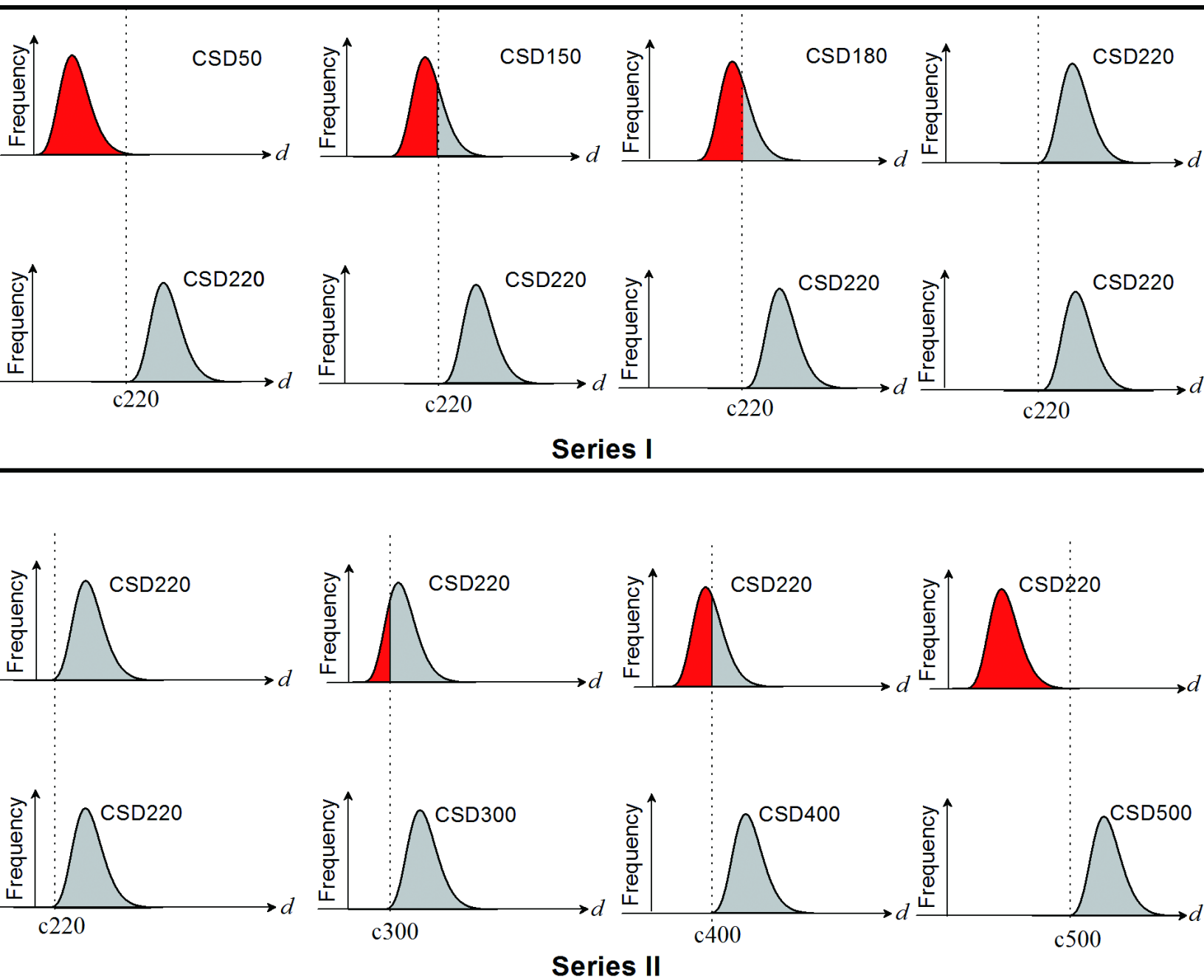


Figure 13

